

Dynamic Response of Wigner Crystals

Lili Zhao, Wenlu Lin, and Yang Liu*

International Center for Quantum Materials, Peking University, Haidian, Beijing 100871, China

Yoon Jang Chung, Adhuth Gupta, Kirk W. Baldwin, and Loren N. Pfeiffer

Department of Electrical Engineering, Princeton University, Princeton, New Jersey 08544, USA

The Wigner crystal, an ordered array of electrons, is one of the very first proposed many-body phases stabilized by the electron-electron interaction. This electron solid phase has been reported in ultra-clean two-dimensional electron systems at extremely low temperatures, where the Coulomb interaction dominates over the kinetic energy, disorder potential and thermal fluctuation. We closely examine this quantum phase with capacitance measurements where the device length-scale is comparable with the crystal's correlation length. The extraordinarily high performance of our technique makes it possible to quantitatively study the dynamic response of the Wigner crystal within the single crystal regime. Our result will greatly boost the study of this inscrutable electron solid.

Interacting two-dimensional electron system (2DES) subjected to high perpendicular magnetic fields (B) and cooled to low temperatures exhibits a plethora of exotic states [1]. The Wigner crystal (WC) [2] terminates the sequence of fractional quantum Hall states at very small Landau level filling factor [3–24]. This electron solid is pinned by the ubiquitous residual disorder, manifests as an insulating phase in DC transport [3–11], and the electrons' collective motion is evidenced by a resonance in AC transport [12–19]. A series of experiments have been applied to investigate this correlated solid, such as the nonlinear $I - V$ response [4, 16], the noise spectrum [5], the huge dielectric constant [20], the weak screening efficiency [21], the melting process [21–23], the nuclear magnetic resonance [24] and the optics [25, 26].

Capacitance measurements have revealed a series of quantum phenomena [21, 27–38]. In this work, we examine the WC formed in an ultra-high mobility 2DES at $\nu \lesssim 1/5$ using high-precision capacitance measurement [39, 40]. We find an exceedingly large capacitance at low measurement frequency f while the conductance is almost zero. This phenomenon is inconsistent with transporting electrons, but rather an evidence that the synchronous vibration of electrons induces a polarization current. When we increase f , our high-precision measurement captures the fine structure of the resonance response with a puzzling "half-dome" structure. Our systematic, quantitative results provide an in-depth insight of this murky quantum phase.

Our sample consists of an ultra-clean low-density 2DES confined in a 70-nm-wide GaAs quantum well with electron density $n \simeq 4.4 \times 10^{10} \text{ cm}^{-2}$ and mobility $\mu \simeq 17 \times 10^6 \text{ cm}^2/(\text{V}\cdot\text{s})$. Each device has a pair of front concentric gates G1 and G2, whose outer and inner radius are r_1 and r_2 , respectively; see the inset of Fig. 1(a) [41]. We study four devices with $r_1 = 60 \mu\text{m}$ and $r_2 = 60, 80, 100$ and $140 \mu\text{m}$, respectively. We measure the capacitance C and conductance G between the two gates using a cryogenic bridge and analyze its output with a custom-made radio-frequency lock-in amplifier [39–41].

Fig. 1(a) shows the C and G measured from the $r_1 = r_2 = 60 \mu\text{m}$ sample. Both C and G decrease as we increase the magnetic field B , owing to the magnetic localization where the 2DES conductance $\sigma \propto (ne^2\tau)/m^*(1+\omega_c^2\tau^2)$, m^* , ω_c and τ are the effective mass, cyclotron frequency and transport scattering time of the electrons, respectively [40]. The C and G are finite at $\nu = 1/2$ and $1/4$ where the 2DES forms compressible composite Fermion Fermi sea. When ν is an integer or a certain fraction such as $1/3$ and $1/5$, the 2DES forms incompressible quantum Hall liquids so that both C and G vanish [42].

In all the above cases, the current is carried by *transporting electrons*, so that C has a positive dependence on G , i.e. $C \propto G^{3/2}$, as shown in Fig. 1(b) [40]. Such a correlation discontinues when the WC forms at very low filling factors $\nu \lesssim 1/5$, see the blue shaded regions of Fig. 1(a). The vanishing conductance G suggests that the electrons are immovable, however, the surprisingly large capacitance C evidences that the WC hosts a current even surpassing the conducting Fermi sea at $\nu = 1/2$ and $1/4$ at much lower magnetic field! The phase transition between the WC and the liquid states are clearly evidenced by spikes in G (marked by solid circles in Fig. 1(a)) and sharp raises in C . A developing minimum is seen in G at $1/5 < \nu < 2/9$ (marked by the up-arrow) when C has a peak. This G minimum develops towards zero and the C peak saturates when the solid phase is stronger (see black traces in Fig. 3(a)). This is consistent with the reentrant insulating phase [3–5, 16, 19, 43, 44].

It is important to mention that the 2DES in our devices is effectively "isolated" and we are merely transferring charges between different regions within one quantum phase. Similar to the dielectric materials which also have no transporting electrons, the collective motion of all electrons, i.e. the $k \rightarrow 0$ phonon mode of WC, can generate *polarization charges* and corresponding polarization current in response to the in-plane component of applied electric field. An infinitesimally small but ubiquitous disorder pins the WC so that electrons can

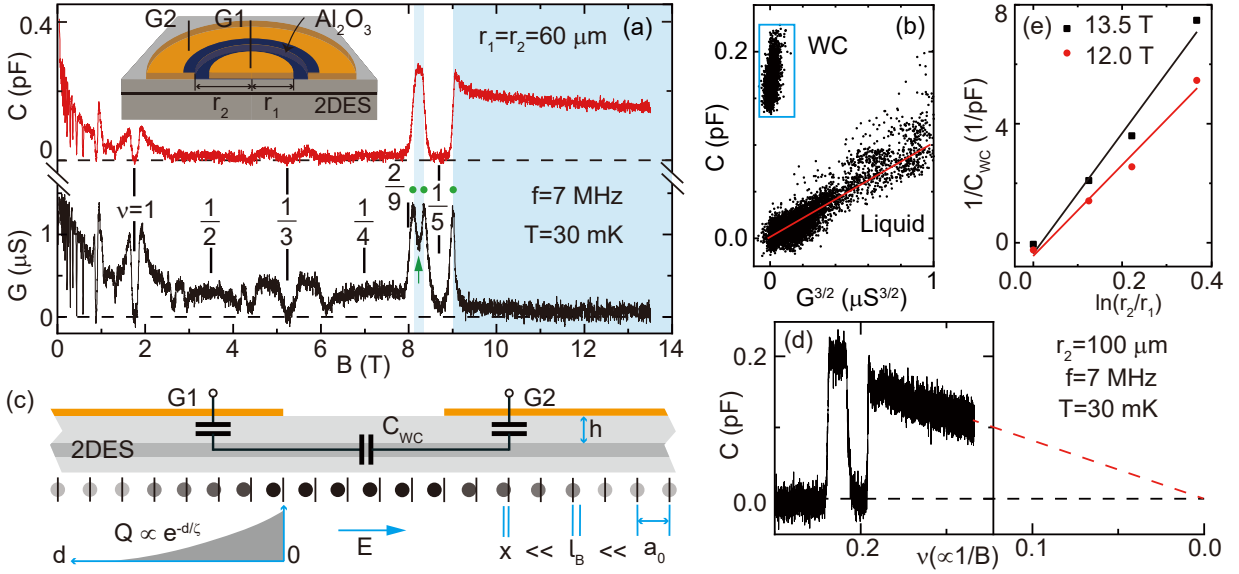


FIG. 1. (color online) (a) C and G measured from the $r_1 = r_2 = 60 \mu\text{m}$ sample with 7 MHz excitation at 30 mK. The horizontal dashed lines represent the zeros of C or G . The blue shaded regions mark the presence of WC. Inset is the cartoon of our device. (b) The correlation between C and G in panel (a) data. Transporting current dominates at $B < 8 \text{ T}$ where $C \propto G^{3/2}$, indicated the red solid line. When the WC polarization current dominates, $C \simeq 0.2 \text{ pF}$ and G is about zero (the blue box). (c) The schematic model describing the collective motion of electrons in the pinned WC. h is the depth of 2DES. The equally spaced (by the lattice constant a_0) vertical bars represent the equilibrium position of electrons. The darker gray corresponds to larger electron displacement represent the electron position at finite external electric field \mathbf{E} . The gray-scaled solid circles represent the electron position at finite external electric field \mathbf{E} . The radius of individual electron is about the magnetic length l_B . The accumulated charge Q is proportional to $\nabla \cdot \mathbf{x}$, and decays exponentially as a function of the distance d from the gate boundary. ζ is the decay length. C_{WC} is the effective capacitance of WC in the un-gated region between the two gates. (d) C v.s. ν of the $r_2=100 \mu\text{m}$ sample. The black dashed line is the zero of C . The red dashed line is the linear extension of data, showing that $C = 0$ at the extreme quantum limit $\nu = 0$. (e) $1/C_{\text{WC}}$ v.s. $\ln(r_2/r_1)$ at two different magnetic field.

only be driven out of their equilibrium lattice site by a small displacement \mathbf{x} , as shown in Fig. 1(c). During the experiments, we use excitation $V_{\text{in}} \simeq 0.1 \text{ mV}_{\text{rms}}$ and the measured WC capacitance is $\sim 0.15 \text{ pF}$ at 13.5 T. The polarization charge accumulated under the inner gate is $Q = CV_{\text{in}} \sim 100 e$. The corresponding electron displacement at the boundary of the inner gate, $|\mathbf{x}(r_1)| \simeq Q/(2\pi r_1 n e) \sim 0.6 \text{ nm}$, is much smaller than the magnetic length $l_B = \sqrt{\hbar/eB} \sim 8 \text{ nm}$, substantiating our assumption that the electrons vibrate diminutively around their equilibrium lattice sites.

An ideal, disorder-free WC is effectively a perfect dielectric with infinite permittivity, so that the device capacitance should be close to its zero-field value $C_0 \sim 1 \text{ pF}$ when 2DES is an excellent conductor. We note that C_0 is consistent with the device geometry, $\epsilon_0 \epsilon_{\text{GaAs}} \pi r_1^2 / h \simeq 1.3 \text{ pF}$, where $\epsilon_{\text{GaAs}} = 12.8$ is the relative dielectric constant of GaAs and $h \simeq 960 \text{ nm}$ is the depth of 2DES. However, the measured $C \sim 0.15 \text{ pF}$ in the WC regime is much smaller than C_0 . This discrepancy is likely caused by the friction-like disorder which poses a pinning force $\simeq -\beta \mathbf{x}$ on the electrons. When the crystal's inversion symmetry is broken, i.e. \mathbf{x} is non-uniform and $\mathcal{J}(\mathbf{x})$ is finite, the electron-electron interaction generates a restor-

ing force $\simeq -a_0 \mu_{ij} \mathcal{J}(\mathbf{x})$, where μ_{ij} , a_0 and $\mathcal{J}(\mathbf{x})$ are the elastic tensor, WC lattice constant and the Jacobi matrix of \mathbf{x} , respectively. At the low frequency limit, the WC is always at equilibrium and all forces are balanced, $e\mathbf{E} - a_0 \mu_{ij} \mathcal{J}(\mathbf{x}) - \beta \mathbf{x} = 0$, \mathbf{E} is the total parallel electric field on the WC.

\mathbf{E} is approximately zero under the metal gates, since the gate-to-2DES distance h is small. Therefore, \mathbf{x} decreases exponentially when the distance from the gate boundary d increases, $\mathbf{x} \propto \exp(-d/\zeta)$, where $\zeta = \mu a_0 / \beta$ is the decay length. Deeply inside the gates, electrons feel neither parallel electric field nor net pressure from nearby electrons, so that their displacement \mathbf{x} remains approximately zero. This region does not contribute to the capacitive response, and the effective gate area reduces to about $2\pi r_1 \zeta$ and $2\pi r_2 \zeta$ at the inner and outer gate, respectively. Because $r_1 = r_2 = 60 \mu\text{m}$ in Fig. 1(a), the experimentally measured $C \approx \epsilon_0 \epsilon_{\text{GaAs}} / h \cdot 2\pi r_1 \zeta / 2 \simeq 0.15 \text{ pF}$ at 13.5 T corresponds to a decay length $\zeta \simeq 6.7 \mu\text{m}$. Interestingly, our result shows a linear dependence $C \propto 1/B$ in Fig. 1(d), suggesting that $\beta \propto l_B^{-2}$ if we assume μ_{ij} is independent on B . Especially, the pinning becomes infinitely strong, i.e. $\beta \rightarrow \infty$, at the extreme quantum limit $l_B \rightarrow 0$.

The permittivity of a disorder-pinned WC is no longer infinitely large, since a non-zero electric field \mathbf{E} is necessary to sustain a finite \mathbf{x} . If we assume \mathbf{x} is a constant in the ring area between the two gates, so that $e\mathbf{E} = \beta\mathbf{x}$. The residual \mathbf{E} can be modeled as a serial capacitance $C_{\text{WC}} \approx 2\pi ne^2/\beta \cdot [\ln(r_2/r_1)]^{-1}$ in our device. We then measure different devices with $r_1 = 60 \mu\text{m}$ and $r_2 = 60, 80, 100$ and $140 \mu\text{m}$, and calculate the corresponding C_{WC} through $C_{\text{WC}}^{-1} = C^{-1} - (r_1 + r_2)/r_2 \cdot C_{r_1=r_2}^{-1}$, see Fig. 1(e). By fitting the linear dependence $C_{\text{WC}}^{-1} \propto \ln(r_2/r_1)$, we estimate the pinning strength β to be about 1.3×10^{-9} and 1.1×10^{-9} N/m at $B = 13.5$ and 12 T, respectively [45]. Finally, assuming $\mu_{ij} \approx \mu \cdot \delta_{ij}$, we can estimate the WC elastic modulus $\mu \approx \beta \cdot \zeta/a_0$. For example, μ is about 1.6×10^{-7} N/m at 13.5 T.

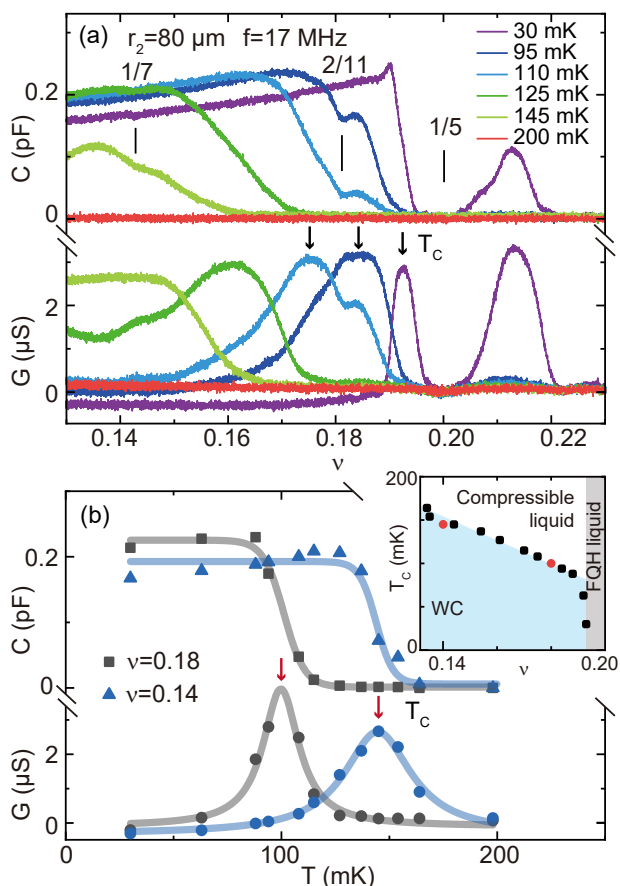


FIG. 2. (color online) (a) C and G vs. ν measured at various temperatures from the $r_2 = 80 \mu\text{m}$ sample with 17 MHz excitation. (b) Summarized C and G vs. T at $\nu = 0.14$ and 0.18 from the panel (a) data. A critical temperature T_c at certain ν is defined either as the temperature when G has a peak at ν in panel (a) or as the temperature when G vs. T trace reaches maximum in panel (b); marked by the black and red arrows. The panel (b) inset summarizes the T_c using the two equivalent definitions using black and red circles, respectively. The diagram can be separated into three different regions corresponding to the WC, the fractional quantum Hall (FQH) liquid and the compressible liquid.

Fig. 2 reveals an intriguing temperature-induced solid-liquid phase transition when the WC melts. Fig. 2(a) shows C and G taken from the $r_2 = 80 \mu\text{m}$ sample at various temperatures. At a certain temperature, e.g. at $T \approx 110$ mK, $C \sim 0.2$ pF when the 2DES forms WC at $\nu \lesssim 0.16$ and vanishes when it is a liquid phase at $\nu \gtrsim 0.18$. G has a peak at $\nu \simeq 0.175$ when C vs. ν has the maximal negative slope, and it is small when the 2DES is either a WC at $\nu < 0.17$ or a liquid at $\nu > 0.19$ [46]. At very high temperature $T \gtrsim 200$ mK, both C and G are close to zero. In Fig. 2(b), we summarized C and G as a function of T at two different filling factors to better illustrate this solid-liquid transition. At $\nu \simeq 0.14$, for example, C is large and G is small at $T \lesssim 100$ mK when the WC is stable [47], while both of them become small at $T \gtrsim 200$ mK when the 2DES is a liquid. The G has a peak at a critical temperature T_c , marked by the red arrows, around which the precipitous decrease of C happens. Alternatively, T_c at a certain filling factor ν can be defined as the temperature when the G has a peak (black arrow in Fig. 2(a)) at ν . We summarize T_c obtained using these two equivalent procedures in the Fig. 2(b) inset with corresponding red and black symbols. T_c has a linear dependence on ν whose two intercepts are $T_c \simeq 340$ mK at the extreme quantum limit $\nu = 0$, and $\nu \simeq 1/4$ at $T_c = 0$ mK.

The Fig. 2(b) evolution can be qualitatively understood by the coexistence of transport and polarization currents at the solid-liquid transition. The large C reduces to almost zero when the transport current dominates over the polarization current. G is a measure of the 2DES's capacity to absorb and dissipate power. It is negligible if either of these two currents dominates, since the polarization current is dissipation-less and the dissipating transport current is difficult to excite. G becomes large when these two currents coexist nip and tuck at intermediate T when the excited polarization charge can be just dissipated by the transport current.

The WC exhibits a resonance when we increase the excitation frequency. In Fig. 3(a), the C and G measured from the $r_2 = 100 \mu\text{m}$ sample using different excitation frequencies change enormously when the WC presents (blue shaded region). G is almost zero and C is large at $f \simeq 7$ MHz, and G becomes finite and C becomes even larger at $f \simeq 23$ MHz. At slightly higher frequency 27 MHz, G reaches its maximum and C drops to about zero. Further increasing f , G gradually declines while C first becomes negative at 35 MHz and then gradually approaches zero. The summarized C and G vs. f at two certain fillings in Fig. 3(b), resembles qualitatively a resonant behavior with resonance frequency $f_r \simeq 26$ MHz (when $C = 0$). Fig. 3(c) studies this resonance at different temperatures. The data is taken from the $r_2 \simeq 80 \mu\text{m}$ sample whose resonance frequency is about 35 MHz [48]. The abrupt change of C near f_r becomes gradual and the G peak flattens at higher temperatures.

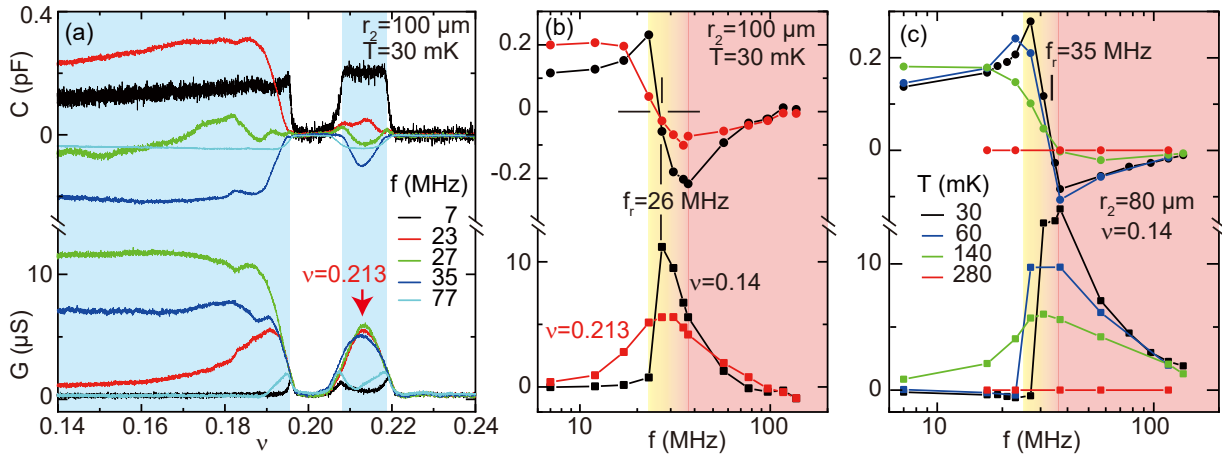


FIG. 3. (color online) (a) C and G vs. ν taken from the $r_2=100 \mu\text{m}$ sample using different excitation frequencies f . We see a violent change of C and G at different f in the blue region where the WC appears. (b) The C and G vs. f extracted from the panel (a) trace at $\nu = 0.14$ and 0.213 . The resonance frequency f_r , defined as the frequency when C changes its sign, is about 26 MHz . (c) The C and G vs. f at $\nu = 0.14$ and different temperatures, data taken from the $r_2=80 \mu\text{m}$ sample. The resonance disappears at $T \simeq 280 \text{ mK}$ when C and G remain nearly zero.

Both C and G become flat zero at $T \gtrsim 280 \text{ mK}$. It is noteworthy that, as long as a resonance is seen, f_r is nearly independent on the filling factor (Fig. 3(b)) and temperatures (Fig. 3(c)). This is consistent with another experimental study using surface acoustic wave [23].

The resonance of WC is usually explained by the pinning mode [18, 49]. The resonance frequency is related to the mean free path L_T of the transverse phonon through $L_T = (2\pi\mu_{t,cl}/neBf_r)^{1/2}$, where $\mu_{t,cl} = 0.245e^2n^{3/2}/4\pi\epsilon_0\epsilon_{\text{GaAs}}$ is the classical shear modulus of WC. $f_r = 26 \text{ MHz}$ corresponds to $L_T \simeq 3.2 \mu\text{m}$, very similar to $\zeta \simeq 6.7 \mu\text{m}$ in our Fig. 1(c) discussion. This is justifiable because both L_T and ζ describe the length-scale within which the collective motion of WC is damped/scattered by the random pinning potential.

Before ending the discussion, we would like to highlight the puzzling "half-dome" structure of the resonance. G has a regular-shaped resonance peak, i.e. G decreases gradually on both sides of f_r , when either the WC is weak ($\nu \simeq 0.213$ in Fig. 3(b)) or the temperature is high ($T \simeq 140 \text{ mK}$ in Fig. 3(c)). Surprisingly, the resonance peak becomes quite peculiar when the WC is strong at $\nu \simeq 0.14$ and $T \simeq 30 \text{ mK}$. G gradually decreases from its peak at f_r on the high frequency side $f > f_r$, while it vanishes instantly when the frequency is lower than f_r , resulting in a "half-dome" G vs. f trace. Meanwhile, the C increases by ~ 2 times and then abruptly changes to negative at f_r . This anomalous "half-dome" feature is seen in all of our devices as long as the WC is strong and temperature is sufficiently low, suggesting a threshold frequency for the power dissipation.

In conclusion, using the extraordinarily high-precision capacitance measurement technique, we investigate the dynamic response of WC systematically. From the quan-

titative results and using a simple model, we can study several physical properties of the WC such as elastic modulus, dielectric constant, pinning strength, etc., and discover a puzzling "half-dome" feature in the resonance peak. Our results certainly shine light on the study of WC and provides new insight on its dynamics.

We acknowledge support by the National Nature Science Foundation of China (Grant No. 92065104 and 12074010) and the National Basic Research Program of China (Grant No. 2019YFA0308403) for sample fabrication and measurement. This research is funded in part by the Gordon and Betty Moore Foundation's EPIQS Initiative, Grant GBMF9615 to L. N. Pfeiffer, and by the National Science Foundation MRSEC grant DMR 2011750 to Princeton University. We thank L. W. Engel, Bo Yang and Xin Lin for valuable discussion.

* liuyang02@pku.edu.cn

- [1] J. K. Jain, *Composite Fermions* (Cambridge University Press, Cambridge, UK, 2007).
- [2] E. Wigner, *Phys. Rev.* **46**, 1002 (1934).
- [3] H. W. Jiang, R. L. Willett, H. L. Stormer, D. C. Tsui, L. N. Pfeiffer, and K. W. West, *Phys. Rev. Lett.* **65**, 633 (1990).
- [4] V. J. Goldman, M. Santos, M. Shayegan, and J. E. Cunningham, *Phys. Rev. Lett.* **65**, 2189 (1990).
- [5] Y. P. Li, T. Sajoto, L. W. Engel, D. C. Tsui, and M. Shayegan, *Phys. Rev. Lett.* **67**, 1630 (1991).
- [6] M. B. Santos, Y. W. Suen, M. Shayegan, Y. P. Li, L. W. Engel, and D. C. Tsui, *Phys. Rev. Lett.* **68**, 1188 (1992).
- [7] T. Sajoto, Y. P. Li, L. W. Engel, D. C. Tsui, and M. Shayegan, *Phys. Rev. Lett.* **70**, 2321 (1993).
- [8] W. Pan, H. L. Stormer, D. C. Tsui, L. N. Pfeiffer, K. W. Baldwin, and K. W. West, *Phys. Rev. Lett.* **88**, 176802

- (2002).
- [9] D. Maryenko, A. McCollam, J. Falson, Y. Kozuka, J. Bruin, U. Zeitler, and M. Kawasaki, *Nature Communications* **9**, 4356 (2018).
- [10] M. S. Hossain, M. K. Ma, K. A. V. Rosales, Y. J. Chung, L. N. Pfeiffer, K. W. West, K. W. Baldwin, and M. Shayegan, *Proceedings of the National Academy of Sciences* **117**, 32244 (2020).
- [11] Y. J. Chung, D. Graf, L. W. Engel, K. A. V. Rosales, P. T. Madathil, K. W. Baldwin, K. W. West, L. N. Pfeiffer, and M. Shayegan, *Phys. Rev. Lett.* **128**, 026802 (2022).
- [12] Y. Lozovik and V. Yudson, *JETP Lett.* **22**, 11 (1975).
- [13] P. K. Lam and S. M. Girvin, *Phys. Rev. B* **30**, 473 (1984).
- [14] D. Levesque, J. J. Weis, and A. H. MacDonald, *Phys. Rev. B* **30**, 1056 (1984).
- [15] E. Y. Andrei, G. Deville, D. C. Glattli, F. I. B. Williams, E. Paris, and B. Etienne, *Phys. Rev. Lett.* **60**, 2765 (1988).
- [16] F. I. B. Williams, P. A. Wright, R. G. Clark, E. Y. Andrei, G. Deville, D. C. Glattli, O. Probst, B. Etienne, C. Dorin, C. T. Foxon, and J. J. Harris, *Phys. Rev. Lett.* **66**, 3285 (1991).
- [17] C.-C. Li, L. W. Engel, D. Shahar, D. C. Tsui, and M. Shayegan, *Phys. Rev. Lett.* **79**, 1353 (1997).
- [18] P. D. Ye, L. W. Engel, D. C. Tsui, R. M. Lewis, L. N. Pfeiffer, and K. West, *Phys. Rev. Lett.* **89**, 176802 (2002).
- [19] Y. P. Chen, R. M. Lewis, L. W. Engel, D. C. Tsui, P. D. Ye, Z. H. Wang, L. N. Pfeiffer, and K. W. West, *Phys. Rev. Lett.* **93**, 206805 (2004).
- [20] Y. Li, D. Tsui, T. Sajoto, L. Engel, M. Santos, and M. Shayegan, *Solid State Communications* **95**, 619 (1995).
- [21] H. Deng, L. N. Pfeiffer, K. W. West, K. W. Baldwin, L. W. Engel, and M. Shayegan, *Phys. Rev. Lett.* **122**, 116601 (2019).
- [22] Y. P. Chen, G. Sambandamurthy, Z. H. Wang, R. M. Lewis, L. W. Engel, D. C. Tsui, P. D. Ye, L. N. Pfeiffer, and K. W. West, *Nature Physics* **2**, 452 (2006).
- [23] I. L. Drichko, I. Y. Smirnov, A. V. Suslov, Y. M. Galperin, L. N. Pfeiffer, and K. W. West, *Phys. Rev. B* **94**, 075420 (2016).
- [24] L. Tiemann, T. D. Rhone, N. Shibata, and K. Muraki, *Nature Physics* **10**, 648 (2014).
- [25] Y. Zhou, J. Sung, E. Brutschea, I. Esterlis, Y. Wang, G. Scuri, R. J. Gelly, H. Heo, T. Taniguchi, K. Watanabe, G. Zaránd, M. D. Lukin, P. Kim, E. Demler, and H. Park, *Nature* **595**, 48 (2021).
- [26] T. Smoleński, P. E. Dolgirev, C. Kuhlenkamp, A. Popert, Y. Shimazaki, P. Back, X. Lu, M. Kroner, K. Watanabe, T. Taniguchi, I. Esterlis, E. Demler, and A. Imamoglu, *Nature* **595**, 53 (2021).
- [27] V. Mosser, D. Weiss, K. Klitzing, K. Ploog, and G. Weimann, *Solid State Communications* **58**, 5 (1986).
- [28] R. C. Ashoori, H. L. Stormer, J. S. Weiner, L. N. Pfeiffer, S. J. Pearton, K. W. Baldwin, and K. W. West, *Phys. Rev. Lett.* **68**, 3088 (1992).
- [29] T. P. Smith, W. I. Wang, and P. J. Stiles, *Phys. Rev. B* **34**, 2995 (1986).
- [30] M. J. Yang, C. H. Yang, B. R. Bennett, and B. V. Shanabrook, *Phys. Rev. Lett.* **78**, 4613 (1997).
- [31] J. P. Eisenstein, L. N. Pfeiffer, and K. W. West, *Phys. Rev. B* **50**, 1760 (1994).
- [32] A. A. Zibrov, C. Kometter, H. Zhou, E. M. Spanton, T. Taniguchi, K. Watanabe, M. P. Zaletel, and A. F. Young, *Nature* **549**, 360 (2017).
- [33] H. Irie, T. Akiho, and K. Muraki, *Applied Physics Express* **12**, 063004 (2019).
- [34] J. P. Eisenstein, L. N. Pfeiffer, and K. W. West, *Phys. Rev. Lett.* **68**, 674 (1992).
- [35] J. Jo, E. A. Garcia, K. M. Abkemeier, M. B. Santos, and M. Shayegan, *Phys. Rev. B* **47**, 4056 (1993).
- [36] L. Li, C. Richter, S. Paetel, T. Kopp, J. Mannhart, and R. C. Ashoori, *Science* **332**, 825 (2011).
- [37] A. A. Zibrov, P. Rao, C. Kometter, E. M. Spanton, J. I. A. Li, C. R. Dean, T. Taniguchi, K. Watanabe, M. Serbyn, and A. F. Young, *Phys. Rev. Lett.* **121**, 167601 (2018).
- [38] S. L. Tomarken, Y. Cao, A. Demir, K. Watanabe, T. Taniguchi, P. Jarillo-Herrero, and R. C. Ashoori, *Phys. Rev. Lett.* **123**, 046601 (2019).
- [39] L. Zhao, W. Lin, X. Fan, Y. Song, H. Lu, and Y. Liu, *Review of Scientific Instruments* **93**, 053910 (2022).
- [40] L. Zhao, W. Lin, Y. J. Chung, K. W. Baldwin, L. N. Pfeiffer, and Y. Liu, *Chinese Physics Letters* **39**, 097301 (2022).
- [41] See Supplemental Material for detailed description of our sample information and measurement techniques.
- [42] The zero of C and G can be defined either by extrapolating their field dependence to $B = \infty$, or by their values at strong quantum hall states such as $\nu = 1$. These two approaches are consistent with each other and the dash lines in Fig. 1(a) represent the deduced zero.
- [43] M. Shayegan, in *High Magnetic Fields: Science and Technology*, Vol. 3, edited by F. Herlach and N. Miura (World Scientific, Singapore, 2006) pp. 31–60.
- [44] M. Shayegan, in *Perspectives in Quantum Hall Effects*, edited by S. D. Sarma and A. Pinczuk (Wiley, New York, 1998) pp. 343–383.
- [45] Alternatively, C_{WC} can be modeled as a cylinder capacitor whose height equals the effective thickness of the 2DES, $Z_0 \approx 45$ nm. The WC dielectric constant is $\epsilon_{WC} = (2\pi\epsilon_0 Z_0 \partial(C_{WC}^{-1})/\partial \ln(r_2/r_1))^{-1} \approx 2 \times 10^4$ at 13.5 T, consistent with previous reported value in ref. [20].
- [46] We observe developing minimum at $\nu = 1/7, 2/11$ during the solid-liquid phase transition, signaling that the fractional quantum Hall state emerges [8, 11].
- [47] C vs. T has a slightly positive slope in the WC region, possibly due to the softening of disorder pinning.
- [48] f_r has no obvious dependence with sample geometry, which is about 35, 35, 26 and 29 MHz for samples with $r_2 = 60, 80, 100, 140$ μm , respectively.
- [49] M. M. Fogler and D. A. Huse, *Phys. Rev. B* **62**, 7553 (2000).

SUPPLEMENTARY MATERIALS

Samples

The sample we studied is made from a GaAs/AlGaAs heterostructure wafer grown by molecular beam epitaxy. A 70 nm-wide GaAs quantum well is bound by AlGaAs spacer-layers and δ -doped layers on each side, and locates $h \simeq 960$ nm below the sample surface. The as-grown density of the 2DES is $n \simeq 4.4 \times 10^{10} \text{ cm}^{-2}$, and its mobility at 300 mK is $\mu \simeq 17 \times 10^6 \text{ cm}^2/(\text{V}\cdot\text{s})$. Our sample is a 2 mm \times 2 mm square piece with four In/Sn contacts at each corner. The contacts are grounded through a resistor to avoid signal leaking. We evaporate concentric, Au/Ti front gate pair G1 and G2 using standard lift-off process, whose outer and inner radius is r_1 and r_2 , respectively. We deposit a 20 nm thick Al_2O_3 layer between the two gates to prevent them from shorting with each other. The four outer-gates are merged into one piece so that the area of the outer gate G2 is much larger than the inner gate G1.

Capacitance Measurement Setup

The capacitance and conductance response is measured with a cryogenic bridge similar to refs. [39, 40].

The kernel of the bridge consists four devices, R_h , R_r , C_r and C , as shown in Fig. S1(a). C is the capacitance of sample. We change the value of R_h to reach the balance condition

$$\frac{C}{C_r} = \frac{R_h}{R_r}. \quad (1)$$

The bridge output V_{out} is minimum at the balance condition, from which we calculate the C . This is the so-call ‘‘V-curve’’ procedure, see refs. [39, 40] for more information.

In order to expand the allowed bandwidth of the excitation frequency, we add an impedance match network to the input of the bridge, shown as the Fig. S1(a). V_{ext} is the signal source with 50 Ω output impedance. V_{ext} drives a signal splitter box (the red dashed box) located at the top of the dilution refrigerator through a ~ 2 m-long semi-rigid coaxial cable. The box input is a 1:5

transformer in series with a 50 Ω resistor. The transformer output drives two serial connected 50 Ω resistors differentially. The differential signals are transmitted to the cryogenic sample holder (the blue dotted box) by two rigid coaxial cables of ~ 2 m length. Another pair of impedance matching 50 Ω resistors are added at the input of the cryogenic bridge, and the 360 Ω resistors are chosen by balancing the competition between the performance and heating. The characteristic impedance of all coaxial cables in the work is 50 Ω .

The low-frequency signals $V_{\text{quasi-DC1}}$ and $V_{\text{quasi-DC2}}$ used to measure the value of R_h and R_r , respectively. The 0.1 μF capacitors are used to separate the high-frequency excitation signals and the quasi-DC signal.

The output V_{out} is approximately

$$V_{\text{out}} \propto S \cdot \left(\frac{R_h}{360 + R_h} - \frac{C}{C_r} \cdot \frac{R_r}{360 + R_r} \right) \cdot V_{\text{ext}}. \quad (2)$$

S can be obtain from the ‘‘V-curve’’ procedure by linear fitting the V_X vs. $R_h/(360 + R_h)$, as shown in Fig. S1(b). V_X and V_Y are the orthogonal component of V_{out} ,

$$\begin{cases} V_X = |V_{\text{out}}| \cdot \cos(\theta), \\ V_Y = |V_{\text{out}}| \cdot \sin(\theta), \end{cases} \quad (3)$$

where θ is the phase of V_{out} . We can derive the value of C using Eq. (2) and (3). The new balance condition of the revised bridge is

$$\frac{C}{C_r} = \frac{R_h}{R_r} \cdot \frac{360 + R_r}{360 + R_h}, \quad (5)$$

where the $V_X = 0$.

Note that the capacitance C and the conductance G of sample lead to the orthogonal component V_X and V_Y , respectively. Therefore, the G can be obtained from Eq. (2) and (4) by replacing C/C_r with $G/2\pi f C_r$, where f is the excitation frequency.

Fig. S1(c) shows our calibration measurement using different excitation frequencies. The data is almost flat from 7 to ~ 100 MHz. The measured capacitance begins to decline slowly above ~ 100 MHz, possibly due to the parasitic inductance of bonding wires.

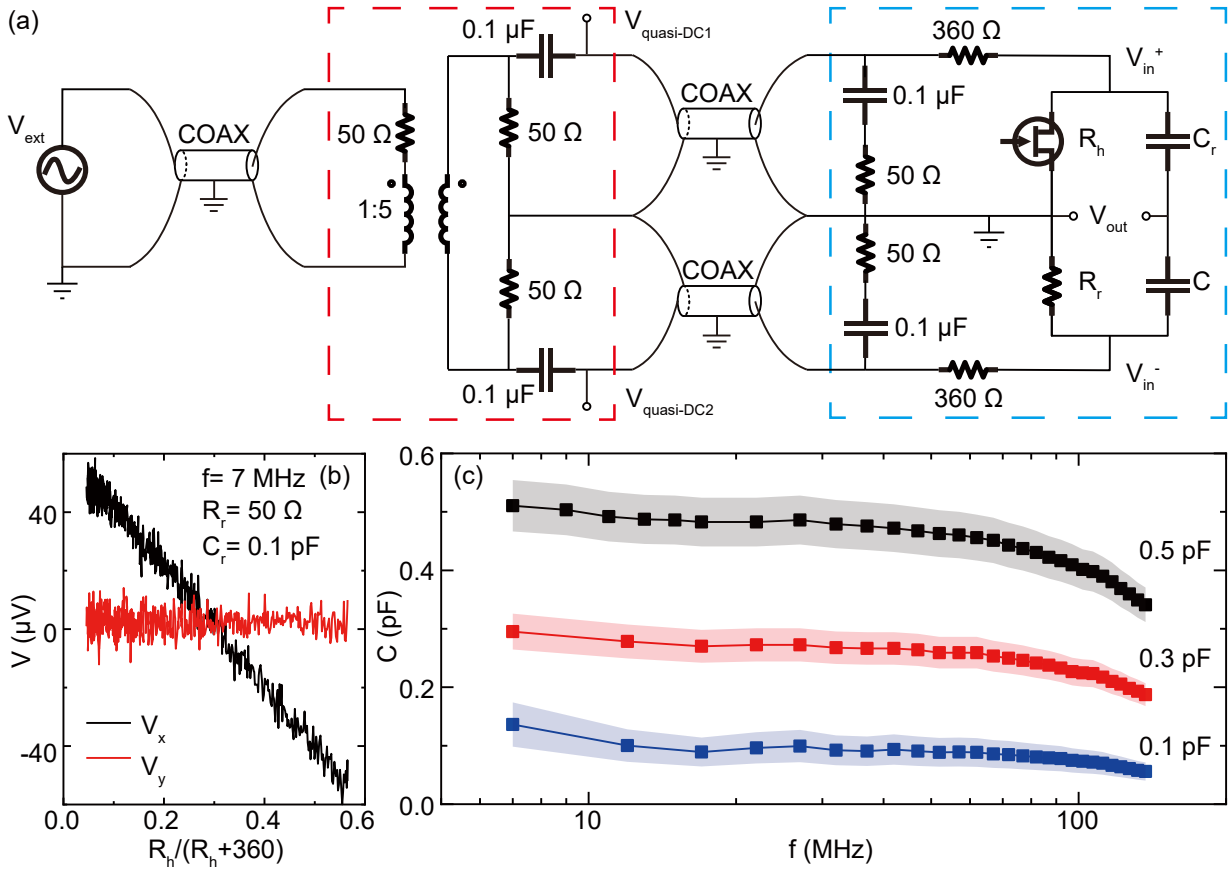


FIG. S1. (color online) (a) Circuit diagram of measurement bridge with $50\ \Omega$ impedance match networks. (b) The V_x and V_y from a typical “V-curve” procedure. C is about $0.25\ \text{pF}$ from the balance condition Eq. (5). (c) The calibration results, by measuring commercial capacitors with different frequencies.